PCCP

Cite this: *Phys. Chem. Chem. Phys.*, 2011, **13**, 18015–18022

www.rsc.org/pccp

PAPER

Hemispherical nanobubbles reduce interfacial slippage in simple liquids

Anne Finger and Diethelm Johannsmann*

Received 13th May 2011, Accepted 17th August 2011
DOI: 10.1039/c1cp21548e

Using an electrochemical quartz crystal microbalance (EQCM), we have produced bubbles of nanoscopic size at the front electrode of an acoustic shear wave resonator. Nanobubbles are usually expected to increase the resonance frequency because they have a low density and, also, because a liquid slides easily at a liquid–air interface. However, the bubble-induced frequency shift in many cases was negative, which implies positive hydrodynamic thickness and *reduced* slippage. The explanation is based on Laplace pressure. Due to the bubbles' inherent stiffness, the space in-between neighboring bubbles may turn into an assembly of pockets which move with the underlying substrate in the same way as a solid film. If, first, the bubbles are so small that the Laplace pressure can overcome the viscous drag, and, second, the contact angle is in the range of 90°, the latter effect dominates. This interpretation was corroborated by a calculation using the finite element method (FEM). The argument as such is not limited to acoustic shear waves: hemispherical nanobubbles increase the surface drag in stationary flows in the same way.

I Introduction

Slippage at a solid–liquid interface has for a long time been regarded as a classic misunderstanding. As the textbooks explain, the solid–liquid interface obeys a no-slip condition because the interactions between small molecules and the wall should be at least as strong as the interactions between two such molecules in the bulk.[1,2] The effective viscosity at the interface therefore should be at least as large as the bulk viscosity. There are many examples of enhanced viscosity ("solidified layers") near a solid–liquid interface. These are composed of immobilized molecules. The opposite phenomenon, a layer of highly mobile molecules, was considered an exception, if not a phantom.

Today there is solid experimental evidence for slip even in simple liquids.[3–5] On a fundamental level, there is agreement that (nano-)bubbles can—under certain circumstances—facilitate the lateral movement of liquid.[6] For instance, a hydrophobic sphere impinging onto a water surface through air dives deeper into the liquid than the same sphere hitting the same surface, when the air is replaced with water vapor. This is explained by a thin film of gas at the surface of the sphere.

We briefly mention two other meanings of slip, which are *not* covered here. Slip can mean "*solid-like sliding*" in the sense of friction and tribology.[7] While such phenomena can definitely be investigated with shear wave resonators,[8] they are outside the scope of this work. Secondly, slip can mean interfacial shear thinning in *complex liquids*.[9] The well-known everyday-example is tooth paste. When squeezed out of the tube, tooth paste experiences plug flow because the large stress at the wall induces structural transformations inside the paste (such as an alignment of polymer chains along the direction of shear). These make the boundary less viscous than the bulk. Acoustic shear waves are not well suited to study such effects. Complex fluids usually are so viscous that they overdamp the shear vibration. A second problem with slip in complex fluids is the large stress required to induce structural changes at the interface.

Slip in simple liquids is of practical relevance whenever there is flow on small spatial scales. The most obvious example is flow in porous media,[10] where the pore size may easily be of the same order of magnitude as the slip length (for the definition of the slip length see Fig. 1). A second example is sedimentation,[11] where the slip length must be compared to the particle diameter. Although not much appreciated in the literature, nanobubbles and slip should be of outstanding importance in electrochemistry. Gas diffusion electrodes[12] and electrophoretic deposition are examples.[13] The work reported here was carried out using high frequency acoustic waves because the associated short wavelengths make it easy to detect slip. In a practical context, such conditions are found in ultrasonic cleaning[14] and sonoelectrochemistry.[15] This is not to say that the arguments outlined below are irrelevant to steady flows. The behavior of hemispherical nanobubbles in steady flow is very similar to their behavior in ultrasonic shear fields.

The paper is structured as follows. In Section II, we briefly remind the reader of the simplest possible model of slip and what this model predicts for the frequency shift obtained with a quartz crystal microbalance (QCM). Sections III and IV

Institute of Physical Chemistry, Clausthal University of Technology, Arnold-Sommerfeld-Str. 4, D-38678 Clausthal-Zellerfeld, Germany. E-mail: johannsmann@pc.tu-clausthal.de

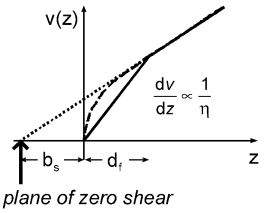

Fig. 1 Flow profile above a solid surface with slip. The slope, $dv(z)/dz$, is inversely proportional to the local viscosity, $\eta(z)$. From Newton's law of action, the shear stress is constant and independent of z. Solid line: the viscosity is reduced inside a hypothetical discrete layer of thickness d_f. Dashed line: the viscosity $\eta(z)$ increases continuously from a small value at the surface to a somewhat higher value in the bulk. At the surface, the shear gradient is increased correspondingly. The slip length, b_s, is the distance from the surface to the extrapolated plane of zero shear (dotted line).

describe the experimental methods and the results obtained in an electrochemical context. Section V explains qualitatively, why nanobubbles may *increase* the hydrodynamic resistance at an interface, rather than inducing slip. Section VI complements the explanation put forward in Section V with a finite element analysis and Section VII concludes.

II A simple model of slip and its consequences for the frequency shift of a QCM

The continuum model of slip in simple liquids amounts to a layer of decreased viscosity close to the surface. Decreased viscosity implies increased shear gradient. The slip length, b_s, (see Fig. 1) is defined by extrapolating the linear portion of the flow profile, $v(z)$, to the plane of zero shear. Should the plane of zero shear be located below the interface, then the distance between the two is called slip length.[16] Evidently, the near-surface viscosity may also be increased. Reasons might be surface roughness, the presence of adsorbates, or an increased density. The distance between the surface and the plane of zero shear then is the hydrodynamic thickness of the respective layer.[17] The slip length can be viewed as an apparent negative hydrodynamic thickness. One can show that the slip length, b_s, is given by[5]

$$b_s = \left(\frac{\eta_{liq}}{\eta_f} - 1\right) d_f \qquad (1)$$

d_f is the thickness of the layer with reduced viscosity (solid line in Fig. 1) and η_f is the viscosity inside this layer. Since eqn (1) is linear in d_f, it also holds for continuous profiles $\eta(z)$ (dashed line in Fig. 1) in an integral sense:

$$b_s = \int_0^\infty \left(\frac{\eta_{liq}}{\eta(z)} - 1\right) dz \qquad (2)$$

The term "slip length" does not involve a statement what-so-ever on the physical origin of slippage. It only rephrases the phenomenon.

For simple liquids one expects the layer of anomalous viscosity (be it decreased or increased) to be a few nanometres (a few molecules) thick, at most. Unless the viscosity in the denominator of eqn (2) is close to zero, the slip length is a few nm, as well, and the measurement of the slip length by conventional macroscopic techniques therefore is difficult. As has been pointed out by numerous authors, acoustic waves should be well-suited tools of investigation.[18–20] The depth of penetration of the acoustic shear wave emanating from the resonator is around 100 nm. If the slip length is—for instance—1% of the penetration depth, slip is readily observable in acoustic experiments.

When employing acoustic resonators, one typically relies on changes of the resonance frequency and the bandwidth. There is a simple relation between the frequency shift, Δf, and b_s if the slip layer is much thinner than the wavelength of sound ("long wavelength-approximation"). In the following, we present a simplified treatment. For more complete accounts see ref. 18–20. We treat the slipping layer as an acoustic multilayer, where each layer, i, is characterized by its thickness, d_i, its acoustic impedance, Z_i, and its speed of transverse sound, c_i. The wave vector, k_i, is given by ω/c_i. Since $k_i d_i \ll 1$ for all layers, trigonometric functions in $k_i d_i$ can be linearized, whenever they occur. Making these approximations, one finds[21]

$$\begin{aligned}\frac{\Delta f^*}{f_F} &\approx -\frac{-\omega}{\pi Z_q}\sum_i \frac{Z_i^2 - Z_{liq}^2}{Z_i^2}\rho_i d_i \\ &\approx -\frac{-\omega}{\pi Z_q}\int_0^\infty \frac{Z^2(z) - Z_{liq}^2}{Z^2(z)}\rho(z)\mathrm{d}z \\ &\approx -\frac{\rho_{liq}\omega}{\pi Z_q}\int_0^\infty \frac{G(z) - G_{liq}}{G(z)}\mathrm{d}z \\ &\approx -\frac{\rho_{liq}\omega}{\pi Z_q}\int_0^\infty \frac{\eta(z) - \eta_{liq}}{\eta(z)}\mathrm{d}z\end{aligned} \qquad (3)$$

Here $\Delta f^* = \Delta f + i\Delta\Gamma$ is the complex frequency shift and $\Delta\Gamma$ is shift of the half bandwidth at half maximum ("bandwidth", for short). Many users of the QCM-D describe dissipative processes by the parameter D ("dissipation") instead of Γ. The two are related by $D = 2\Gamma/f$. $f_F = 5$ MHz is the frequency of the fundamental, $Z_q = 8.8 \times 10^6$ kg m^{-2} s^{-1} is the acoustic impedance of AT-cut quartz. $Z(z) = (\rho(z)G(z))^{1/2}$ is the acoustic impedance of the material at position z, ρ is the density, and G is the shear modulus. The index liq denotes the liquid. Constant density ($\rho \sim \rho_{liq}$ everywhere) was assumed in line 2. $G = i\omega\eta$ was used in the last line.

If the viscosity of the film is much larger than the viscosity of the liquid, the integrand in eqn (3) becomes unity and eqn (3) reduces to the Sauerbrey equation.[22] If, on the other hand, $\eta(z)$ is lower than η_{liq}, Δf becomes positive and is proportional to the slip length. To see this, write:

$$\begin{aligned}\frac{\Delta f}{f_F} \approx -\frac{\rho_{liq}\omega}{\pi Z_q}\int_0^\infty \frac{\eta(z) - \eta_{liq}}{\eta(z)}\mathrm{d}z &\approx \frac{2f\rho_{liq}}{Z_q}\int_0^\infty \left(\frac{\eta_{liq}}{\eta(z)} - 1\right)\mathrm{d}z \\ &= \frac{2f}{Z_q}\rho_{liq} b_s\end{aligned} \qquad (4)$$

To the experimentalist, slip looks like a negative Sauerbrey mass, where the slip length is the same as the apparent negative Sauerbrey thickness. Since frequency, f, is proportional to overtone order, n, eqn (4) predicts $\Delta f/n$ = const. The latter relation is referred to as "Sauerbrey scaling" in the following.

Rigid films (“Sauerbrey films”) have the same dependence of Δf on n (albeit with negative Δf).

Positive frequency shift upon bubble evolution *has* been observed in the past. To our knowledge, the first report is from the Hillman group.[23] These authors produced bubbles of molecular hydrogen and molecular chlorine in an electrochemical QCM. At large negative and large positive voltages (cathodic and anodic conditions, respectively) the frequency strongly increased. From today’s perspective, their Fig. 3 is intriguing, because the frequency shift in the intermediate regime (low voltage) is by no means a flat horizontal line. Rather, there were *negative* frequency shifts when the voltage was ramped from zero towards the anodic and the cathodic region. Possibly, the Hillman group saw nanobubbles in the sense of Fig. 5a. Zhang also reports positive frequency shifts caused by nanobubbles.[24] These experiments were not of electrochemical nature. Rather, nanobubbles were produced by the solvent exchange procedure.[25] With such bubbles, there has been intense debate on whether or not these are stable and, if so, why.[26] We do not contribute to this debate. In our work, bubbles are the consequence of a dynamic equilibrium between the formation of molecular hydrogen at the cathode and its dissolution. Positive Δf upon bubble formation is—somewhat on the side—mentioned in ref. 27. In this work, the focus was on the electrochemistry of IO_3^- and the evidence for bubble formation is not strong. Rather, the positive frequency shift was considered as an indication of bubble formation. The Craig group used nanobubbles to clean protein-covered surfaces.[28] Again, the frequency shift is positive. Finally, there is an interesting and carefully performed study on electrochemically produced bubbles and the extent to which these lead to slip.[29] Interestingly, the experimental results remained inconclusive. The frequency shift was below the noise level.

The results shown below are of a similar kind as the ones reported in ref. 29. In particular, we have seen many examples, where we expected nanobubble formation and did not see corresponding changes in frequency or bandwidth. All experiments carried out in acids were of this type. Only after we switched to salt solutions at neutral pH did we see the results shown in the Experimental section. Furthermore, there was a dependence of Δf and $\Delta\Gamma$ on the type of salt employed. Presumably this goes back to an influence of the salt onto the wettability of the substrate. The details of the conditions under which nanobubbles form are outside the scope of this work. Again: these nanobubbles are not at all stable, but rather the result of a dynamic equilibrium. They disappear once the cathodic voltage is turned off. They are not of the peculiar type of nanobubbles found with the solvent exchange procedure.[25] In the following, we first describe the experiment (Section III) and show the experimental results (Section IV). These experiments suggest that bubbles may appear as solid-like objects. This is rationalized on a qualitative basis in Section V. Section VI further corroborates this argument with a finite element calculation.

III Experimental

The experiments were carried out with 5 MHz crystals purchased from Fil-Tech (Boston, MA). They were coated with gold and an adhesive layer of chromium. The diameter was one inch. They were mounted in a commercial holder supplied by Maxtek Inc., CA. Organic contaminants were removed from the gold electrodes prior to experiment by means of a UV-ozone cleaner (Bioforce Nanoscience Inc., Ames, IA). When reusing the crystals between different experiments, we thoroughly washed them in ultrapure water. Frequency and bandwidth were determined by classical impedance analysis.[30] The network analyzer employed was the unit HP4396 from Hewlett Packard, CA.

The instrument was operated as a classical electrochemical QCM (EQCM). A three-electrode-setup was employed with the front electrode of the quartz crystal acting as the working electrode, a platinum sheet as the counter electrode, and a saturated calomel electrode (SCE, Sensortechnik Meinsberg, Germany) as the reference. The voltage of the working electrode, φ, was controlled by a potentiostat (PGU 10V-1A IMP, Jaissle, Germany) connected to a function generator (33220A, Agilent Technologies Inc., CA). φ was alternated between 0 V *vs.* SCE and a negative voltage (−0.5 to −1.8 V in steps of 0.1 V, see Fig. 2). The duration was 2 min for each voltage setting. All water was of ultrapure grade (18.2 MΩ cm, Sartorius arium 611VF). The electrolytes were 1 mol L^{-1} solutions of the respective salts in water. KNO_3 (Riedel-de Haën, p.A.), NaCl (Aldrich, ACS reagent), and NaBr (Acros Organics, p.A.) were used as received.

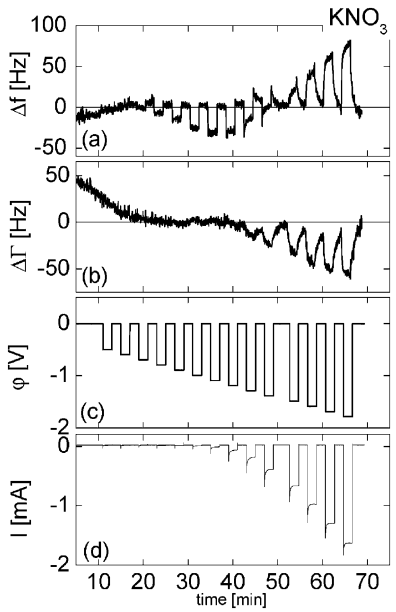

Fig. 2 Evolution of frequency (a), bandwidth (b), and electrochemical current (d) with time upon subjecting the sample to negative voltage pulses of 2 minutes duration and variable height. The voltage trace is panel c. The variation in Δf in the initial phase of the experiment is a drift of the baseline. The threshold voltage for nanobubble formation (as evidenced by a nonzero Δf) is −0.6 V *vs.* SCE. At this voltage, the current is in the range of a few μA. The bandwidth, $\Delta\Gamma$, hardly responds. At voltages more negative than −1 V *vs.* SCE, the picture changes. The frequency shift becomes positive, $\Delta\Gamma$ turns negative (comparable in magnitude to the shift in Δf) and the current increases to values in the range of 1 mA. This happens because now macrobubbles form at the crystal surface, also easily observed by eye.

IV Results

Fig. 2 shows a data trace obtained with KNO_3 as the supporting electrolyte. There are several noteworthy features. First, and most importantly, the frequency shift observed upon application of a voltage to the cathode was stable and negative for φ between -0.6 V and -1 V. For electrode potentials of $\varphi < -1.5$ V, Δf is clearly positive. In the latter case, there were significant drifts of Δf *during* the pulse. Bubbles were visible. Note: the visible bubbles were *macro*bubbles. Only these were visible to the eye, nanobubbles were not. The macrobubbles grew in size until they detached from the surface and floated to the top of the cell. In the intermediate voltage range (-1 to -1.5 V), Δf was poorly reproducible and we do not discuss the details.

Fig. 3 shows the dependence of Δf (at 15 MHz) on potential, φ, for three different types of supporting electrolytes. In all three cases, Δf eventually turns positive at $\varphi < -1.5$ V. However, Δf is not always negative at the less negative voltages (-0.5 V $< \varphi < -1$ V). It is positive in this range for NaBr. Following the arguments outlined at the end of Section V, this should be interpreted as a consequence of either high or low air–water contact angles. In the former case, the bubble forms a shallow lens which hardly deviates the flow. In the latter case, the bubble is a truncated sphere which responds to the flow by rotation with little deformation.

Even though there is no experimental evidence, the stability criterion speaks in favor of a shallow bubble. If the contact line is pinned (it usually is to some degree) and the bubble is shallow, the curvature of the air–water interface increases with increasing bubble volume. The saturation concentration of dissolved gas in the liquid phase then increases as well according to the Kelvin equation[31] and the rate of dissolution increases, in consequence. This eventually limits the further growth of the bubble. For truncated spheres this feed back loop works the other way: the rate of dissolution decreases as the bubble radius increases, which leads to self-accelerating growth.

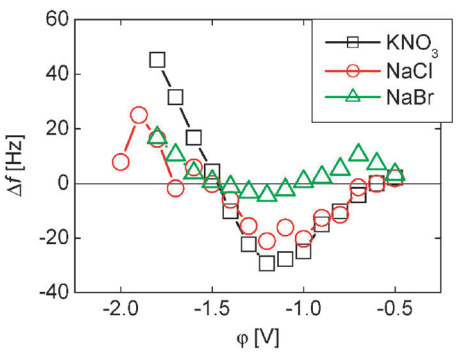

Fig. 3 Frequency shifts of the 3rd harmonic *versus* the cathodic voltage for three different supporting electrolytes. The salt concentration was 1 mol L^{-1} in all cases. The frequency shift is positive at large negative voltages, because ultimately, the cathodic voltage produces macrobubbles. Interestingly, Δf is not always negative at potentials less negative than -0.5 V. For NaBr, it is positive. Following Fig. 5b, we explain this finding with either a large or a small contact angle (shallow bubble or bubble forming a truncated sphere, respectively).

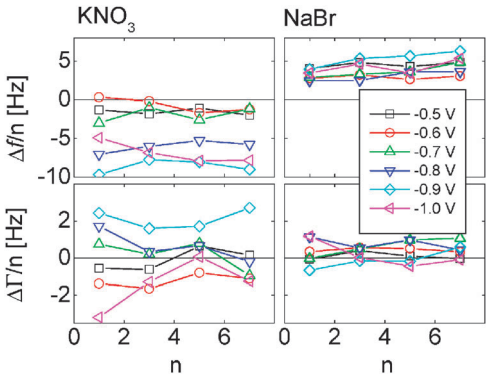

Fig. 4 Normalized frequency shifts, $\Delta f/n$, and normalized shifts of bandwidth, $\Delta\Gamma/n$, *versus* n. Δf and $\Delta\Gamma$ were time-averaged over the duration of the pulse. The voltages are indicated in the legend. For both KNO_3 and NaBr, the overtone dependence of the frequency shift is best approximated by $\Delta f/n \approx$ const., that is, by Sauerbrey scaling. The layer of bubbles looks solid-like in the case of KNO_3, whereas it constitutes a slip layer (*cf.* eqn (4)) in the case of NaBr.

Fig. 4 shows the dependence of the time-averaged shifts of $\Delta f/n$ and $\Delta\Gamma/n$ on n. For both KNO_3 and NaBr, $\Delta f/n$ is about constant, which amounts to Sauerbrey scaling. As far as the case of $\Delta f > 0$ is concerned, this matches the prediction from eqn (4). For the case of $\Delta f < 0$, one might also expect that the amount of trapped mass is independent of overtone order. The experiment supports this conjecture.

V Bubbles may appear as stiff objects

The explanation for a bubble-induced increase in coupled mass follows from the notion that bubbles (and nanobubbles, in particular) may be viewed as stiff objects due to the deformation-induced Laplace pressure. Bubbles can speed up the movement of the nearby liquid relative to the situation on a flat surface. Bubbles in this sense create surface roughness, which increases the moving mass.

Consider the deformed bubble depicted in Fig. 5a. The curvature of the interface has decreased on the left-hand side, while it has increased on the right. The change in curvature is proportional to the bubble deformation (in units of %) and to the curvature of the undeformed bubble, $1/r_0$.

Bubble deformation *per se* is a complicated subject.[32,33] Consider stationary flows, first. There is rule of thumb for small deformation. In this limit the deformation (defined as the normalized change in length of the long axis, $\Delta L/L$) is proportional to the capillary number, Ca, where the latter is defined as

$$Ca = \frac{\dot{\gamma}\eta r_0}{\sigma} \qquad (5)$$

$\dot{\gamma}$ is the shear rate (or, more generally, the characteristic rate of the flow) and σ is the surface tension. Ca compares the viscous stress, $\dot{\gamma}\eta$ to the Laplace pressure, σ/r_0. Bubble deformation has an associated time scale, termed "emulsion time" in the context of droplets.[32] It is given as $\tau_r = \eta r_0/\sigma$. After cessation of flow, the bubbles return to a spherical shape within a time about equal to τ_r. The capillary number can also be written as $Ca = \dot{\gamma}\tau_r$. Written this way, Ca compares the flow rate to the

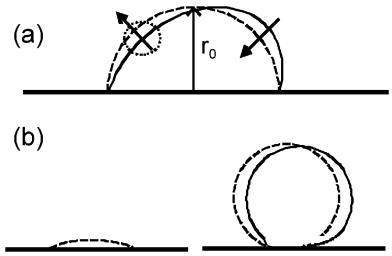

Fig. 5 Illustration of the forces connected to bubble deformation. Panel a shows a hemispherical bubble. Under shear, a Laplace pressure of magnitude $\sigma\Delta(1/r)$ develops at the deformed surfaces. Here $1/r$ is the curvature, $\Delta(1/r)$ is the shear-induced change in curvature, and σ is the surface tension. Arrows indicate deformation-induced forces. Panel b depicts two bubble geometries, which do *not* increase the apparent mass. If the bubble is shallow, the liquid easily flows around it. Most of the interfacial flow is tangential and the bubble lowers the interfacial shear stress. If, on the other hand, the bubble forms a truncated sphere (lower right), there is normal stress at the interfaces, but the bubble can accommodate for it by rotation rather than deformation.

inverse emulsion time. As long as $\dot{\gamma} < \tau_r^{-1}$, the flow-induced elongation is—within numerical factors of order unity—equal to Ca. The flow-induced change in curvature then is

$$\Delta\left(\frac{1}{r}\right) \approx \frac{1}{r_0} Ca = \frac{\eta}{\sigma}\dot{\gamma} \qquad (6)$$

Again, we have disregarded numerical coefficients. The flow-induced normal pressure is

$$p_{\mathrm{norm}} = \sigma\Delta\left(\frac{1}{r}\right) \approx \eta\dot{\gamma} \qquad (7)$$

Note that only the flow-induced *changes* in the Laplace pressure affect the flow. The static Laplace pressure is irrelevant for the bubble's dynamical behavior. As eqn (7) shows, the normal pressure exerted by the deformed bubble is of the same order of magnitude as the viscous stress. Whether bubbles increase or decrease the hydrodynamic drag at a surface depends on the numerical factors, which cannot be easily predicted from simple arguments. Our claim that bubbles may increase the drag therefore critically relies on the experiment and the FEM calculation. Again, this analysis relies on the condition $Ca \ll 1$. At large flow rates, the bubbles are disrupted and the situation is much different.

As long as $Ca \ll 1$, there is little difference between steady and oscillatory flow. There is one caveat though, which is the need for a bubble radius smaller than the penetration depth of the shear wave, δ. One has $\delta = (2\eta/(\rho\omega))^{1/2}$ with ρ the density of the liquid. For 5 MHz crystals in water, the penetration depth is 250 nm/$n^{1/2}$ (n the overtone order). For ultrasonic shear waves, the shear rate is given as $\dot{\gamma} = \omega u_0/\delta = \omega u_0/\sqrt{2\eta/(\rho\omega)}$. u_0 is the amplitude of oscillation. Eqn (7) now holds in essentially the same way as for steady flow: the bubble-induced stress is about the same as the viscous stress and one needs to look into the details in order to predict whether bubbles enhance or reduce the hydrodynamic drag.

However, a fundamental difference between steady and oscillatory flow occurs for $Ca \gg 1$. In steady flow at $Ca \gg 1$, the situation becomes nonlinear because the bubbles break. At high frequencies, on the other hand, no such nonlinearity occurs because the amplitude is small. For $Ca \gg 1$ in oscillatory flow, the bubbles become *soft* in the sense that their deformation affinely follows the motion of the liquid. If the amplitude was large (which is of course possible, in principle), the bubbles would eventually rupture, but the amplitudes encountered at a QCM-surface never are that large.

In the following, we assume that the bubble shape affinely follows the liquid. When sheared by a small amount, a spherical bubble deforms into an ellipsoid, where the long axis is oriented at an angle of 45° relative to the shear direction. The elongation is the same as the shear angle. The shear angle of the background fluid is u_0/δ. The shear induced change of curvature then becomes

$$\Delta\left(\frac{1}{r}\right) \approx \frac{1}{r_0}\frac{\mathrm{d}u(z)}{\mathrm{d}z} \approx \frac{1}{r_0}\frac{u_0}{\delta} \qquad (8)$$

$u(z)$ is the tangential displacement of the background fluid. In order to estimate whether the bubble significantly deviates the flow, we have to compare the flow-induced normal pressure ($p_{\mathrm{norm}} = \sigma u_0/(r_0\delta)$) to the viscous stress ($\sigma_{\mathrm{visc}} = \dot{\gamma}\eta = \omega u_0\eta/\delta$). One finds

$$\frac{\sigma_{\mathrm{visc}}}{p_{\mathrm{norm}}} \approx \frac{\omega\eta r_0}{\sigma} \qquad (9)$$

Eqn (9) amounts to the definition of characteristic number for high-frequency flows, which plays the same role as the capillary number. We call it Ca^*. Ca^* differs from Ca in that the shear rate, $\dot{\gamma}$, is replaced by frequency, ω. For large Ca^*, the bubble does not rupture, it only becomes soft. At the cross-over between soft and stiff bubbles one has

$$\omega\eta \approx \frac{\sigma}{r_0} \qquad (10)$$

The critical bubble radius below which the flow-induced Laplace pressure exceeds the viscous drag follows from eqn (10). Using $\omega = 2\pi$ 5 MHz (a typical quartz resonator), $\eta = 10^{-3}$ Pa s, and $\sigma \approx 72$ mN m^{-1} (the latter two values mimicking water), the critical radius comes out as 2 μm.

With regard to bubbles larger than this critical radius, one has to bear in mind that the penetration depth of the shear wave is only 250 nm. The shear wave will therefore only deform the lower part of the bubble. In the FEM calculation described below, we intended to keep effects of surface tension and of geometry apart and therefore varied the surface tension, rather than the bubbles size. The bubbles radius was maintained fixed at $r_0 = 10$ nm. With this fixed radius, one calculates the critical surface tension separating "soft" from "stiff" bubbles as $\sigma_c \approx 0.03$ mN m^{-1}.

Still another way of looking at eqn (10) focuses on frequency. Soft and hard bubbles are characterized by $\omega \gg \tau_r^{-1}$ and $\omega \ll \tau_r^{-1}$ respectively. Rather than varying surface tension in the FEM calculation, we might also have varied ω. The short-coming here is that the penetration depth, δ, also depends on ω. In order to ensure $r_0 < \delta$ at all frequencies of interest, the bubble diameter would have to be in the sub-nm range, which of course is unrealistic. Still, conceptually, eqn (9) describes a relaxation.

Importantly, the above considerations are only relevant to the experiment if the contact angle is in the range of 90°. For high and low contact angles (Fig. 5b), flow induced normal pressures do occur, but they are too weak to actually increase the drag at the surface. For shallow bubbles, the liquid easily slides across the bubble surface with little normal stress exerted by the bubble. If, on the other hand, the bubble forms a truncated sphere (to the right in Fig. 5b), the bubbles rotates as a whole with some small amount for deformation at the contact line. It is by no means guaranteed that nanobubbles decrease the resonance frequency. They only do, if they form hemispheres.

VI FEM calculations

Central to the view outlined Section V is the notion that bubbles constitute a heterogeneity.[34] In the following, we analyze this geometry by means of the finite element method (FEM). As described in ref. 35, Δf and $\Delta\Gamma$ can be predicted even for complicated geometries using the finite element method and the small load-approximation (SLA). The latter states that the complex frequency shift $\Delta f^* = \Delta f + i\Delta\Gamma$ is proportional to the area-averaged tangential stress at the resonator surface.

$$\frac{\Delta f^*}{f_F} = \frac{i}{\pi Z_q} Z_L = \frac{i}{\pi Z_q}\frac{\sigma_t}{\dot{u}} \approx \frac{i}{\pi Z_q}\frac{\langle\sigma_t\rangle}{\dot{u}} \qquad (11)$$

$Z_L = \sigma_t/\dot{u}$ is the load impedance, σ_t is the tangential stress, $\dot{u}$ is the tangential velocity and angle brackets denote an area-average. Both σ_t and $\dot{u}$ are to be understood as complex amplitudes of an oscillatory quantity. The SLA is applicable to a wide range of samples. That certainly includes the Sauerbrey film. For the Sauerbrey film, the stress is of inertial origin and given by $m_f(-\omega^2 u_0)$, where m_f is the film's mass per unit area, u_0 is the oscillation amplitude and $-\omega^2 u_0$ is acceleration. The velocity, $\dot{u}$, is given as $i\omega u_0$. Inserting these relations, one finds the Sauerbrey equation[22] ($\Delta f = -2f_F m_f/Z_q$) recovered. Other types of samples produce stress at the crystal surface in various other ways. On a fundamental level, the QCM responds to stress, not to mass. Since Δf^* depends *linearly* on σ_t, the SLA can be applied in an *average* sense. One may replace the stress by an area-averaged stress, $\langle\sigma_t\rangle$. Assume that the sample is a structured material, such as a layer of biological cells, a sand pile, a froth, an assembly of vesicles, or a bubble. If the average stress–velocity ratio at the interface between the resonator and the sample can be calculated in one way or another, a quantitative analysis of the QCM experiment is in reach.

For the FEM calculation, we employed the Incompressible Navier–Stokes module supplied by COMSOL GmbH (Göttingen, Germany). The central limitation of this particular package is the fact that the calculation only covers 2D geometries.[36] The hemicircle in Fig. 6 represents an infinite hemicylinder, rather than a hemisphere. For this reason, the calculation can only be used for qualitative statements.

With regard to the details of the FEM calculation, we refer the reader to ref. 35. Fig. 6 shows the geometry and some raw outputs. The resonator surface is the bottom of the cell. It oscillates tangentially with an amplitude of $u_0 = 0.01$ nm. The cell is 0.8 μm wide and 2 μm high. Only the central portion of the cell is displayed. The top of the cell is an immobile wall. The wall is of little influence on the outcome of the simulation because it is located outside the penetration depth of the shear wave, δ. For a 5 MHz crystal in water, one has $\delta = 250\ \text{nm}/n^{1/2}$. Periodic boundary conditions are applied to the left and to the right. What appears as a single bubble in Fig. 6 therefore is a regularly spaced array of bubbles.

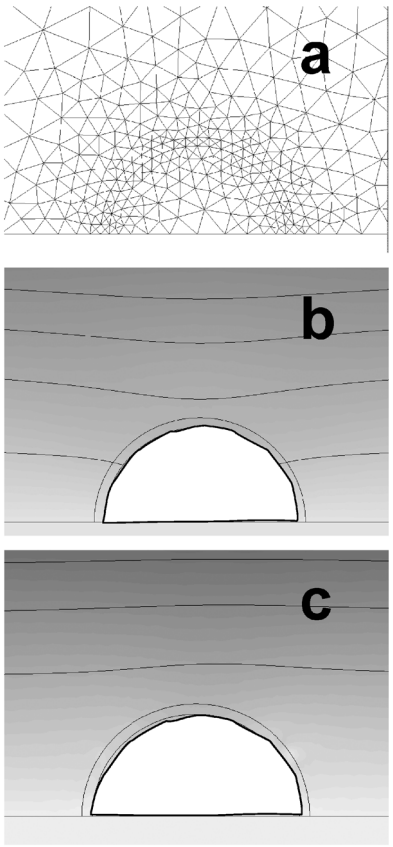

Fig. 6 Panel a shows the geometry of the finite element calculation. The bottom boundary of the cell is the resonator surface, which undergoes tangential oscillations. The hemicircle in the center is the bubble. It is assigned the density and the viscosity of air. The ambient medium is water. The shell in-between air and water is the air–water interface. Its viscosity is the same as the viscosity of water. The low viscosity to the inside amounts to a no-slip condition. Surface tension is incorporated into the model *via* "body forces" onto the membrane. These act in the normal direction and are proportional to the flow-induced change of local curvature. Panels b and c show the lateral velocity as gray values (bright is high velocity), while the lines are the stream lines. In panel b, the interfacial tension was $\sigma = 0.01$ mPa s. The interface is soft under these conditions, and the flow deviates from simple shear flow (which would correspond to horizontal stream lines) in the downward direction. There is a large normal component to the flow at the bubble surface. The liquid deforms the bubble. In the case of high surface tension (panel c, $\sigma = 72$ mPa s), the situation is reversed. The stream lines now deviate upwards. The liquid flows around the bubble, rather than deforming it.

The radius of the bubble in the center is $r_0 = 10$ nm. The contact angle is 90°. The bubble's density and viscosity are 1 kg m^{-3} and 10^{-6} Pa s, respectively. This material mimics air. All materials are assumed to be incompressible. While this is questionable for air, in principle, it is not a problem for

this particular model. Since the wavelength of compressional sound is much larger than the bubble radius, the bubble would have to contract or expand as a whole. Such volume changes are symmetry-forbidden in this particular geometry. Expansion and contraction would have to occur at the same frequency as the tangential oscillation of the substrate. The expansion would therefore have to occur, while the surface moves into one particular direction, but symmetry dictates that the expansion might equally well occur while the substrate moves into the opposite direction. As a consequence, there is no expansion at all.

The liquid–air interface was modeled as a thin layer with density and viscosity the same as of water. Since the air inside the bubble has low viscosity, there are almost no tangential forces acting at the liquid–air interface. The normal forces, on the contrary, are substantial because of surface tension. This is the essence of the model. Surface tension was incorporated into the model in the form of body forces acting onto the material in the thin layer representing the interface. The body forces act in the normal direction and are proportional to the flow-induced change in curvature, $\Delta(1/r)$. $\Delta(1/r)$ was computed as

$$\Delta\left(\frac{1}{r}\right) = \frac{1}{i\omega}\left(\frac{\mathrm{d}^2 v_\mathrm{n}}{\mathrm{d}s^2} - \frac{1}{r_0}\frac{\mathrm{d}v_\mathrm{t}}{\mathrm{d}s}\right) \qquad (12)$$

s is the arc length along the interface. ν_n and ν_t are the normal and the tangential component of the velocity.

Fig. 6b and c show two raw outputs. Gray values encode the local tangential velocity normalized to the velocity of the substrate. The tangential velocity decreases with distance from the resonator surface due to the decay of the shear wave. The lines are streamlines. In Fig. 6b the surface tension was $\sigma = 10^{-5}$ N m^{-1}. Since the Laplace pressure under these conditions almost vanishes, the bubble surface is easily deformed and there is a normal component to the oscillatory flow at the interface. The deviation from pure shear flow is downward. The velocity of flow is reduced above the bubble. This contrasts to the situation depicted in Fig. 6c. Here, the surface tension was $\sigma = 72 \times 10^{-3}$ N m^{-1}, mimicking water. Under these conditions, the streamlines do not cross the liquid–air interface. Rather, they are deviated upwards. The liquid above the bubble moves *faster* than average. The liquid in the pockets is partially locked in its motion to the movement of the substrate by the rigid bubbles.

In order to see the transition from soft to stiff bubbles in the FEM calculation, we varied the surface tension. According to eqn (10), variable surface tension drives the transition between soft and stiff bubbles in essentially the same way as the bubble radius and the frequency, where small surface tension corresponds to large bubbles and high frequency. Fig. 7 shows the derived values of Δf and $\Delta\Gamma$ *versus* surface tension. The surface tension ranged from $\sigma = 10^{-5}$ to 10^{-1} N m^{-1}. The calculation was done for the five lowest harmonics (5, 15, 25, 35, and 45 MHz). Both Δf and $\Delta\Gamma$ were divided by overtone number, n, in order to check for Sauerbrey scaling.

At low surface tension, the frequency shift is positive as predicted by eqn (4). The shift in bandwidth is negative, which is not captured by eqn (4). Eqn (4) is the simplest possible model of slip. More elaborate models[18,19] (not reproduced here) cover changes of dissipation, as well. As the surface tension

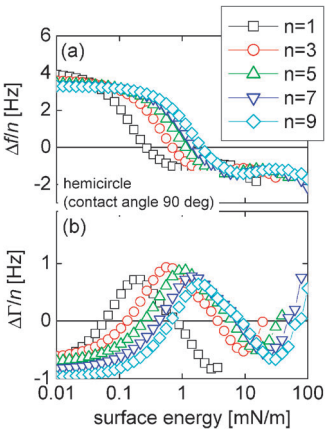

Fig. 7 Normalized shifts of frequency ($\Delta f/n$, a) and bandwidth ($\Delta\Gamma/n$, b) *versus* surface tension as calculated by the finite element method (see Fig. 6). At low surface tension, the frequency shift is positive as predicted by eqn (4). $\Delta\Gamma$ is negative, indicative of a decreased rate of dissipation relative to the semi-infinite liquid. At some critical surface tension (which depends on overtone order) Δf crosses from positive to negative. The features appearing at high surface tensions (to the right) are artifacts originating from the periodicity of the geometry and the corresponding interference effects between the force fields originating from neighboring bubbles.

increases, the frequency shift decreases and turns negative at some critical surface tension, σ_c. As discussed below eqn (10), the value of σ_c should be around 0.03 mM m^{-1}, and should increase with overtone order. This is confirmed by the numerical calculation. At $\sigma \approx \sigma_\mathrm{c}$ the dissipation goes through a maximum. In this respect, the physical situation is analogous to a relaxation. At low surface tension (or, equivalently, high frequency) the bubble is deformable. The deformation is cheap, energetically, and the bubble deformation therefore consumes little energy. At high surface tension (or, equivalently, low frequency), the bubble is rigid. Deformation would be energetically expensive, but it does not happen to any significant extent. Only at intermediate surface tension is the dissipation significant because there is some limited deformation at a significant energetic expense.

At high surface tension the FEM calculation shows some features, which are not of any physical meaning. These resonances go back to an interaction between periodically spaced neighboring bubbles. This is evidenced by the fact that the position of these features on the σ-scale changes with distance between neighboring bubbles (data not shown). Such interference effects are outside the scope of this work.

The FEM model yields Sauerbrey scaling for large and small surface tension. Sauerbrey scaling ($\Delta f/n$ constant, independent of n) is predicted by eqn (4) for the slipping layer. We have argued that the trapped mass in-between bubbles may actually look like a Sauerbrey film. $\Delta f/n$ negative and independent of n is the best scaling we can find for the stiff bubble (high surface tension in Fig. 7a), as well. Sauerbrey scaling was also found in the experiment (Fig. 4).

As stated in Section V, it cannot be easily predicted by simple arguments whether bubbles increase or decrease the hydrodynamic drag at a surface under conditions of $Ca \ll 1$ (or $Ca^* \ll 1$, stiff bubbles). The stress exerted by the bubble is

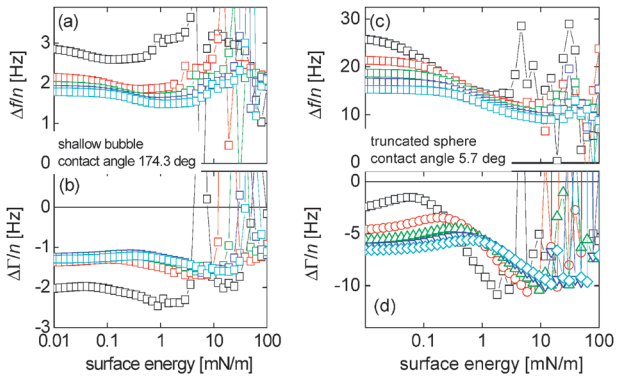

Fig. 8 Shifts of frequency and bandwidth (normalized to overtone order) for a shallow bubble and a bubble which forms a truncated sphere (Fig. 5b). The large values of Δf and $\Delta\Gamma$ seen at high surface tensions are artifacts related to the periodicity of the geometry. In both cases, the frequency shift is positive throughout the entire range of surface energies. One can still see the characteristic features corresponding to relaxation of the bubble shape, but these do not cause Δf to actually reverse sign.

of the same order of magnitude as the viscous stress and one needs to know the numerical coefficients. The FEM calculation amounts to such a quantitative statement. Remember though that the FEM calculation works in 2D. The more important statement here certainly derives from experiment, which leads to the same conclusion as the FEM calculation.

Since the experiments yielded an example where bubbles *did* promote slip (the case where NaBr was employed as the supporting electrolyte) one wonders whether the FEM calculation can catch this situation as well. This is the case. Fig. 8 shows the analog of Fig. 7, where the contact angles were chosen as 174° and 5°. Panels a and b show Δf and $\Delta\Gamma$ for a shallow bubble, panels c and d show Δf and $\Delta\Gamma$ for a truncated sphere (Fig. 5b). For both situations, Δf is positive throughout the entire range of surface tensions. There is a relaxation of similar form as seen in Fig. 7, but the amplitude does not suffice to bring Δf to below zero. These calculations were plagued by interference effects. At high surface tensions, the periodicity of the geometry leads to resonances. These are artifacts. They are seen in Fig. 7 as well, but they are much stronger in Fig. 8. They should be ignored. The emphasis here is on the fact that Δf is positive for all values of σ.

VII Conclusions

Nanobubbles may decrease the frequency shift in a QCM experiment, if the contact angle is around 90°. A negative Δf implies enhanced hydrodynamic drag at the surface. Such conditions were found when producing nanobubbles by electrochemical means on quartz crystal resonators in aqueous solution of KNO_3 and NaCl. Nanobubbles produced in NaBr, on the other hand, produced positive frequency shift, which implies reduced hydrodynamic drag, also referred to as slip.

The explanation is based on the bubble stiffness. Due to the Laplace pressure, bubbles do not significantly deform unless the viscous stress exceeds the deformation-induced Laplace pressure. Stiff bubbles in this sense amount to the condition $\sigma/r_0 > \omega\eta$. At MHz frequencies in water, nanobubbles are rigid objects. Whether they enhance or reduce the drag at the surface depends on the contact angle. If the contact angle is around 90°, they enhance the drag, otherwise they induce slip. Although the measurement was carried out at MHz frequencies, the results should apply to steady flow in the same way. The stiffness condition in steady flow reads as $\sigma/r_0 > \dot{\gamma}\eta$, which implies a small capillary number, Ca. As long as $Ca \ll 1$, hemispherical bubbles increase drag in steady flow, while shallow ones decrease it. This result should be relevant to a wide variety of electrochemical settings.

References

1 D. Bernoulli, *Hydrodynamica*, 1738, 59.
2 R. G. Larson, *The Structure and Rheology of Complex Fluids*, Oxford University Press, 1998.
3 O. I. Vinogradova, *Int. J. Miner. Process.*, 1999, **56**, 31–60.
4 P. A. Thompson and S. M. Troian, *Nature*, 1997, **389**, 360–362.
5 For a review see: C. Neto, D. R. Evans, E. Bonaccurso, H. J. Butt and V. S. J. Craig, *Rep. Prog. Phys.*, 2005, **68**, 2859–2897.
6 D. M. Huang, C. Sendner, D. Horinek, R. R. Netz and L. Bocquet, *Phys. Rev. Lett.*, 2008, **101**, 226101.
7 F. P. Bowden and D. Tabor, *Br. J. Appl. Phys.*, 1966, **17**, 1521.
8 S. Berg and D. Johannsmann, *Phys. Rev. Lett.*, 2003, **91**, 145505.
9 C. L. Tucker and P. Moldenaers, *Annu. Rev. Fluid Mech.*, 2002, **34**, 177–210.
10 B. Lefevre, A. Saugey, J. L. Barrat, L. Bocquet, E. Charlaix, P. F. Gobin and G. Vigier, *Colloids Surf., A*, 2004, **241**, 265.
11 U. C. Boehnke, T. Remmler, H. Motschmann, S. Wurlitzer, J. Hauwede and T. M. Fischer, *J. Colloid Interface Sci.*, 1999, **211**, 243.
12 H. Al-Fetlawi, A. A. Shah and F. C. Walsh, *Electrochim. Acta*, 2009, **55**, 3192.
13 I. Zhitomirsky, *Adv. Colloid Interface Sci.*, 2002, **97**, 279.
14 Q. Qi and G. J. Brereton, *IEEE Trans. Ultrason. Ferroelectr. Freq. Control*, 1995, **42**, 619.
15 R. G. Compton, J. C. Eklund and F. Marken, *Electroanalysis*, 1997, **9**, 509.
16 D. C. Tretheway and C. D. Meinhart, *Phys. Fluids*, 2002, **14**, L9–L12.
17 J. Klein, E. Kumacheva, D. Perahia, D. Mahalu and S. Warburg, *Faraday Discuss.*, 1994, **98**, 173–188.
18 F. Ferrante, A. L. Kipling and M. Thompson, *J. Appl. Phys.*, 1994, **76**, 3448–3462.
19 G. McHale, R. Lucklum, M. I. Newton and J. A. Cowen, *J. Appl. Phys.*, 2000, **88**, 7304–7312.
20 J. S. Ellis and G. L. Hayward, *J. Appl. Phys.*, 2003, **94**, 7856–7867.
21 D. Johannsmann, in *Piezoelectric Sensors*, ed. A. Langhoff and C. Steinem, Springer, Heidelberg, 2006.
22 G. Sauerbrey, *Z. Phys.*, 1959, **155**, 206–222.
23 F. B. Li, A. R. Hillman, S. D. Lubetkin and D. J. Roberts, *J. Electroanal. Chem.*, 1992, **335**, 345–362.
24 X. H. Zhang, *Phys. Chem. Chem. Phys.*, 2008, **10**, 6842–6848.
25 S. T. Lou, Z. Q. Ouyang, Y. Zhang, X. J. Li, J. Hu, M. Q. Li and F. J. Yang, *J. Vac. Sci. Technol., B*, 2000, **18**, 2573–2575.
26 V. S. J. Craig, *Soft Matter*, 2011, **7**, 40–48.
27 Z. L. Li, Z. J. Niu, T. H. Wu, H. D. Nie and X. M. Xiao, *Electrochem. Commun.*, 2003, **5**, 297–300.
28 G. M. Liu, Z. H. Wu and V. S. J. Craig, *J. Phys. Chem. C*, 2008, **112**, 16748–16753.
29 V. Tsionsky, A. Kaverin, L. Daikhin, G. Katz and E. Gileadi, *Phys. Chem. Chem. Phys.*, 2005, **7**, 1830–1835.
30 R. Beck, U. Pittermann and K. G. Weil, *Ber. Bunsen-Ges. Phys. Chem.*, 1988, **92**, 1363–1368.
31 D. Morrison and S. Ross, *Colloidal Dispersions: Suspensions, Emulsions and Foams*, Wiley, 2002.
32 M. Minale, *Rheol. Acta*, 2010, **49**, 789–806.
33 H. A. Stone, *Annu. Rev. Fluid Mech.*, 1994, **26**, 65.
34 B. Y. Du, E. Goubaidoulline and D. Johannsmann, *Langmuir*, 2004, **20**, 10617–10624.
35 D. Johannsmann, I. Reviakine, E. Rojas and M. Gallego, *Anal. Chem.*, 2008, **80**, 8891–8899.
36 The incompressible Navier Stokes module supports 3D calculations, in principle, but when applied to this problem, it produces errors, which we cannot resolve.

